SCIENTIFIC REP🜨RTS

Muon dynamic radiography of density changes induced by hydrothermal activity at the La Soufrière of Guadeloupe volcano

Kevin Jourde[1,2], Dominique Gibert[3,4], Jacques Marteau[2], Jean de Bremond d'Ars[3] & Jean-Christophe Komorowski[1,4]

Imaging geological structures through cosmic muon radiography is a newly developed technique which shows a great potential in volcanology. Here we demonstrate that muon radiography permits to detect and characterize mass movements in shallow hydrothermal systems of low-energy active volcanoes like the La Soufrière lava dome. We present an experiment conducted on this volcano during the Summer 2014 and bring evidence that very important density changes occurred in three domains of the lava dome. Depending on their position and on the medium porosity the volumes of these domains vary from $1 \times 10^6\,\mathrm{m^3}$ to $7 \times 10^6\,\mathrm{m^3}$. However, the total mass budget remains approximately constant : two domains show a mass loss ($\Delta m \in [-0.8; -0.4] \times 10^9\,\mathrm{kg}$) and the third one a mass gain ($\Delta m \in [1.5; 2.5] \times 10^9\,\mathrm{kg}$). We attribute the negative mass changes to the formation of steam in shallow hydrothermal reservoir previously partly filled with liquid water. This coincides with the emergence of new fumaroles on top of the volcano. The positive mass change is synchronized with the negative mass changes indicating that liquid water probably flowed from the two reservoirs invaded by steam toward the third reservoir.

The La Soufrière of Guadeloupe volcano belongs to the Lesser Antilles volcanic arc formed by the subduction of the North American Plate beneath the Caribbean Plate. La Soufrière is the last lava dome in a series of dome extrusions and collapses[1–3]. During the last 8500 years, between 2 and 5 of the 8 collapses that occurred at La Soufrière of Guadeloupe have generated laterally-directed explosions caused by depressurisation (volcanic blasts) of magma and hydrothermal fluids that spread laterally at high speeds (up to $100–235\,\mathrm{m.s.^{-1}}$) over the volcano flanks. These events caused partial collapses and triggered small laterally-directed hydrothermal explosions associated with significant exurgence of hot acid pressurized hydrothermal fluids contained in superficial reservoirs located inside the lava dome[1,4].

The last eruption occurred in 1976–1977 and is considered as a failed magmatic event : a small andesitic magma volume stopped its ascent about 3 km beneath the surface[5,6]. Following this event, degassing, thermal flux and seismicity progressively decreased down to their lowest levels by 1990. By the end of 1992, a resumption of the fumarolic activity at the summit of the dome, of the shallow seismicity, and of the temperature of thermal springs around the dome was observed. In 1998, the sudden onset of high-flux chlorine degassing from the Cratère Sud vent constituted a conspicuous change in the magmatic-hydrothermal system behaviour. In 1997, a small boiling pond formed at the Cratère Sud with extremely acid fluids (minimal pH ≈ -0.8) corresponding to the azeotrope point of hydrochloric acid. A similar larger boiling lake was discovered in 2001 in the Tarissan pit. In 2003, the acid pond at the Cratère Sud was replaced by a strongly degassing vent while Tarissan acid pond continues to exist until now. Since then, a significant increase of the dome fumarolic activity was observed[7–9]. Indeed a new active region appeared to the North-East of the Tarissan pit during the 2014 Summer[8], the North-Napoleon
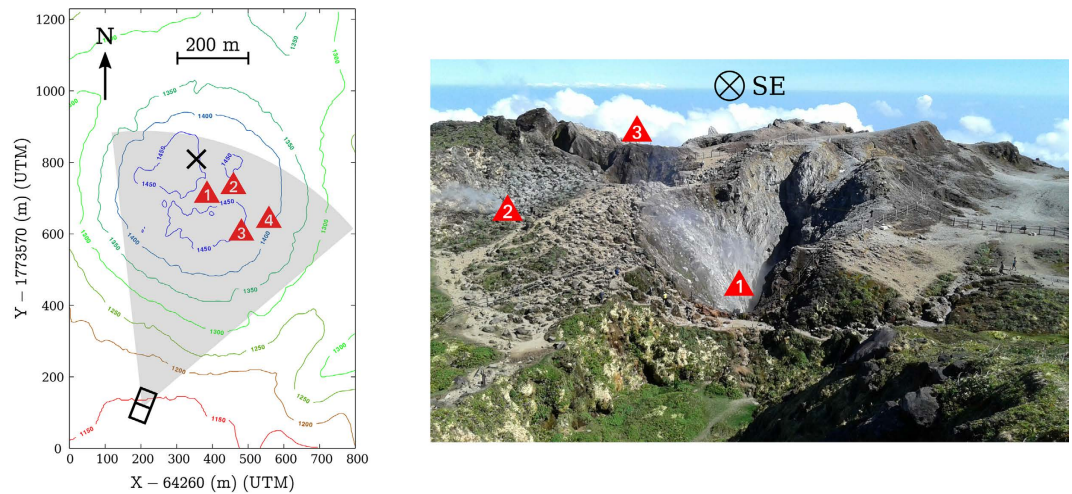
Figure 1. *Left:* **La Soufrière of Guadeloupe topographic map.** The grey surface delimits the region scanned by the muon telescope represented by the black boxes. The red triangles refer to the different active zones visible at the dome surface (1: Tarissan pit, 2: Napoléon-Nord fume, 3: Cratère Sud, 4: Gouffre Breislack and Gouffre 56). *Right:* The La Soufrière's different active vents as seen from the black cross on the left picture.

fumarole, and two old pits, the Gouffre Breislack and the Gouffre 56, have seen their activity rising[9]. All these sites are reported on Fig. 1.

The spatio-temporal evolution of active areas located onto the lava dome may be caused by the progressive sealing of previously active flow paths. This sealing results from the combined effects of hydrothermal activity and heavy rains ($\approx$6–7 m.y^{-1}) that favour fluid mineralization by magmatic gas and the formation of clayey material that progressively fills open fractures. Sealing causes fluid confinement and over-pressurization leading to the opening of new flow paths. The observed increased flux of chlorine-rich vents at the summit and the episodic chlorine spikes recorded in the Carbet and Galion hot springs[6] can be due to the sporadic injection of acid chlorine-rich fluids and heat from the magma reservoir or magma intrusions at depth into the hydrothermal reservoirs[6].

Purely hydrothermal blasts are as mobile as their magmatic counterparts. Small-scale laterally-directed explosions could have caused many fatalities at Tongariro (New-Zealand) in 2012[10–12] and caused 63 fatalities at Ontake volcano (Japan) in 2014[13–16]. In both cases, no clear warning signals were reported. Both the detection of early warning signals, the quantification of both the hydrothermal volumes involved and the amount of energy available, constitute new challenges to modern volcanology. As quoted by several experts who commented the Ontake eruption, theses challenges deserve the development of new techniques providing new data type and of new concepts in data analysis and information processing[13,14,16].

The aim of this paper is to demonstrate the possibility to use muon radiography to monitor density changes in the shallow hydrothermal system inside the lava dome of the La Soufrière of Guadeloupe. As will be shown in the remaining of this paper, we clearly detect density changes related to modifications of the vent activity visible at the volcano's summit. Quantitative attributes like time-constants, concerned volumes and estimates of the amount of thermal energy available may be derived from muon radiography data.

The paper is organized as follows. First, we recall the main principles of cosmic muon radiography. Then we present the experiment performed on the La Soufrière of Guadeloupe during Summer 2014, at the same time that the North-Napoleon fumarole appeared. In a second stage, we present the data and, after eliminating the possibility of artefacts caused by atmospheric perturbations, we provide evidence of large mass movements within the lava dome. Finally, we briefly discuss the consequences for the dynamics of the shallow hydrothermal system.

The muon radiography experiment

Muon radiography aims at recovering the density distribution, ρ, inside the object of interest (in our case the La Soufrière of Guadeloupe) by measuring its screening effect on the cosmic muon flux[17–20]. The material property inferred with muon radiography is the opacity, ϱ [g.cm^{-2}], which measures the amount of matter encountered by the muons along their travel path, L, across the rock mass to image,

$$\varrho = \int_L \rho(l) \times \mathrm{d}l. \tag{1}$$

Muons lose energy through matter by ionisation processes at a typical rate of 2.5 MeV per opacity increment of 1 g.cm^{-2}. The tomography muons we detect are high energy particles ($E_c \gtrsim 50$) we can approximate to travel along straight trajectories for the spatial resolution we are interested in. The muons incident flux is nearly stationary, azimuthally isotropic and mainly depend on the zenith angle[21,22]. Simple flux models can be used to determine the target screening effects[23,22]. These properties have been used for 10 years to image volcanoes internal structures[24,25], and more recently to monitor mass variations linked to their activity[26,27].
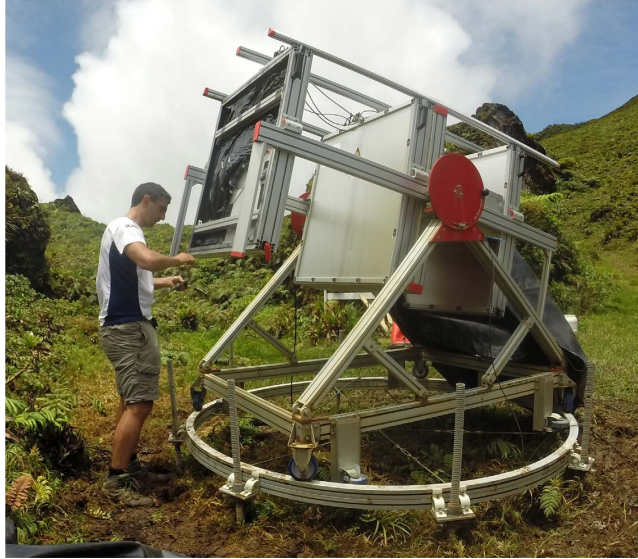
Figure 2. Photography of a muon telescope under maintenance on the La Soufrière of Guadeloupe. The three grey boxes are the three detection matrices. The fourth box, placed just behind the central matrix, contains the telescope steel shielding.

Our cosmic muon telescopes[28] are equipped with 3 plastic scintillator matrices counting 16×16 pixels of $5 \times 5\,cm^2$ (Fig. 2). We set the distance between the front and rear matrices to $140\,cm$ in order to span the entire lava dome from a single point of view (Fig. 1). The combination of pixels defines a total of 31×31 lines of sight with a spatial resolution of about 25 m at the lava dome center. A 7cm–thick steel shielding is placed just behind the center matrix in order to filter background low energy particles from the tomography signal[30–32]. The matrices geometrical arrangement fixes the telescope acceptance function $\mathcal{T}_m$ [cm^2. sr] which controls the flux captured by the instrument on each line of sight $\mathbf{r}_m$. As shown below, the acceptance has a direct influence on the number of muons counted in a given period of time and, consequently, controls the statistical uncertainty of eventual flux variations caused by density changes in the volcano[22,29].

The present dataset runs from July 7th to August 5th and from August 15th to October 10th 2014. The telescope was placed South-South-West at the lava dome basis (Fig. 1), the axial line of sight was oriented $\beta_0 = 25°$ Eastward and the zenith angle set to $\gamma_0 = 75°$ (the telescope is horizontal when $\gamma_0 = 90°$).

We standardized the raw data processing was standardized. Data reduction and filtering include : events time coincidence (on the 3 matrices), particle time-of-flight[33,34], alignment of the fired pixels, number of pixels activated in the rear matrix. This number is larger when particles other than muons (electrons and gamma photons) start showering in the steel shielding. We estimate the resulting background flux to be below 0.05 day^{-1}. sr^{-1}.cm^{-2}), which is good enough to precisely make the discussion section volume and mass computations[30–32] (the article other conclusions can be recovered using only the relative flux time variations). The resulting data set is a sequence $\mathcal{S} = \{e_k, \ k = 1, \cdots, K\}$ of events e_k attributed to cosmic muons arriving in the telescope front. Each event has a time-stamp t_k and is assigned to one particular line of sight $\mathbf{r}_{m(k)}$.

Once obtained, the sequence $\mathcal{S}$ is used to compute the muons number $N_m(t, \Delta t)$ for each line of sight $\mathbf{r}_m$ during a time period Δt. It must be corrected from the acceptance function $\mathcal{T}_m$ to recover the absolute flux $\partial\phi$ and estimate absolute opacity variations.

An additional processing stage specific to the present study (see Methods section below) consists in merging several adjacent lines of sight in order to improve the signal-to-noise ratio. For lines belonging to a subset ε,

$$N_\varepsilon(t, \Delta t) = \sum_{m \in \varepsilon} N_m(t, \Delta t) = \sum_{m \in \varepsilon} \mathcal{T}_m \times \int_{t - \Delta t/2}^{t + \Delta t/2} \partial\phi_m(\zeta)\, d\zeta,$$

(2)

where $\mathcal{T}_m$ and $\partial\phi_m$ are respectively the acceptance function and the absolute flux in the line of sight $\mathbf{r}_m$. Let us precise that more than the telescope geometry, $\mathcal{T}_m$ also depends on the detection efficiency and on the numerical algorithms used to filter the proper events. We evaluate $\mathcal{T}_m$ through a calibration experiment made previously to the tomography measurements. In the following we use $\phi_\varepsilon(t, \Delta_t) = N_\varepsilon(t, \Delta t)/\Delta t$ the particle flux at t, averaged on a Δt time window. As explained in the Methods section, the lines of sight belonging to a given subset ε must share a similar time-variation curve of the muon flux. Such a merging increases the effective acceptance and improves the time resolution. However it induces a decrease in the angular resolution induced by the merging of the small solid angles spanned by the lines of sight.

The telescope mechanical stability is an important issue for monitoring experiments. Changes in the telescope orientation may occur because of the strong mechanical constraints the instrument has to support, especially for measurements under open sky where about 300 kg of steel shielding are necessary as explained above. The ground below the telescope may also slightly move as the Soufrière of Guadeloupe is subject to heavy rains all the year
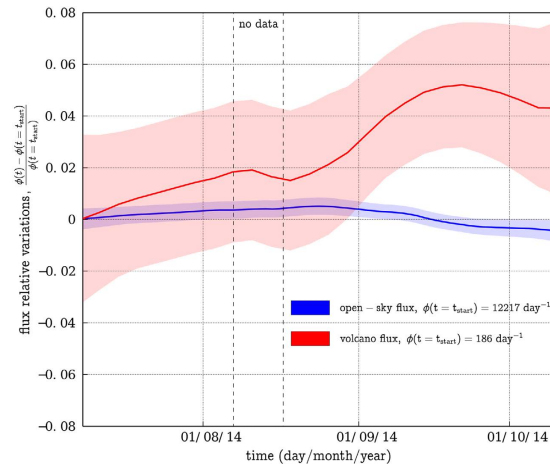
Figure 3. Relative muon flux measured during Summer 2014. In blue: open-sky axes. In red : axes point through the La Soufrière of Guadeloupe volcanic dome. The transparent surfaces associated to each curve delimit the 95% confidence interval. The fluxes are computed using a 30 days large Hamming moving window. The vertical black dotted lines delimit the small period during which the muon telescope was not operational.

long. Periodic checks of both the orientation and inclination of the telescope frame did not reveal any changes during the experiment. The overall telescope acceptance is monitored permanently on the data themselves (using the responses of open-sky oriented lines). No significant changes have ever been observed. This is also confirmed by the Principal Component Analysis (PCA, see Methods section below) used to merge the lines of sight into coherent domains, since it is able to identify and remove global shifts in all lines of sight. Such an effect was not detected during the processing, we thus conclude that no instrumental bias alter the data.

Evidence of opacity changes inside the La Soufrière lava dome

The red curve in Fig. 3 shows the muon flux global relative variations through the La Soufrière lava dome. This curve has been obtained by applying eq. 2 to the subset $\varepsilon_{\text{dome}}$ of all lines of sight that pass through the volcano. The blue curve of Fig. 3 corresponds to the subset ε_{sky} of the lines of sight directed toward the open-sky above the volcano. The transparent surfaces represent the 95% confidence interval. The flux data were smoothed over a 30 days large Hamming window. This smoothing interpolates the data gap delimited by the two vertical black dotted lines. Figure 3 red curve shows a conspicuous increase of about 5% of the muon flux during the whole observation period. Such an increase is not visible in the open-sky flux which instead slightly decreases by about 1% (Fig. 3 blue curve). This indicates that the muon flux increase across the lava dome is likely to be primarily caused by a decrease of the volcano bulk opacity.

In order to identify the locations in the lava dome where the muon flux variations are the most important, we performed a PCA (see Methods section) on all $N_m(t)$ series. The analysis identifies 3 domains where the muon flux time-variations are similar. Each domains lines of sight were merged to compute N_{ε}, $\varepsilon \in \{1, 2, 2^*, 3\}$. ε_{2^*} is a ε_2 subset. We chose it so that it does not have any observation axes in common with ε_1 in order to print ε_2 specific variations. Figure 4 shows the 4 identified domains and their associated muon flux time series. We add a fourth region ε_0 where no variations could be extracted by the PCA analysis and that we show as a control zone. We observe relative variations as large as 20%. We exclude from the PCA instrumental or atmospheric effects which would have impacted all the telescope observation axes. The unambiguous spatial localization and the diversity of the different temporal trends appear to be the strongest argument in favour of explaining the variations by the volcanic activity itself. Statistical considerations concerning time-resolution and potential conclusions on the lava dome hydrothermal activity are briefly discussed in the next two sections.

Atmospheric effects. The cosmic muons are produced in the so-called extended atmospheric showers (EAS) which initiate in the upper atmosphere, at an altitude $z_\mu \approx 15$–20 km, when primary cosmic ray particles (mainly protons) collide with oxygen and nitrogen atoms. When the thermal state of the atmosphere changes, both the air density and z_μ are slightly modified, producing small variations in the muon flux ϕ with respect to its average $\overline{\phi}$. For the present analysis, we use a linear empirical relationship[29,35,36],

$$\frac{\phi - \overline{\phi}}{\overline{\phi}} = \beta_p^* \times (p - \overline{p}) + \alpha_T \times \frac{(T_{\text{eff}} - \overline{T}_{\text{eff}})}{\overline{T}_{\text{eff}}},$$

(3)

where p[hPa] is the ground pressure, $\overline{p}$ the local average ground pressure, $\alpha_T = \beta_T^* \times \overline{T}_{\text{eff}}$ the modulation coefficient and T_{eff} the effective temperature. This temperature is an approximation of T_μ, the atmosphere temperature at the high energy muons production altitude z_μ, not to be misinterpreted with the ground temperature. It corresponds to an estimate of the atmosphere temperature where high-energy muons are produced, at the very beginning of the EAS development.
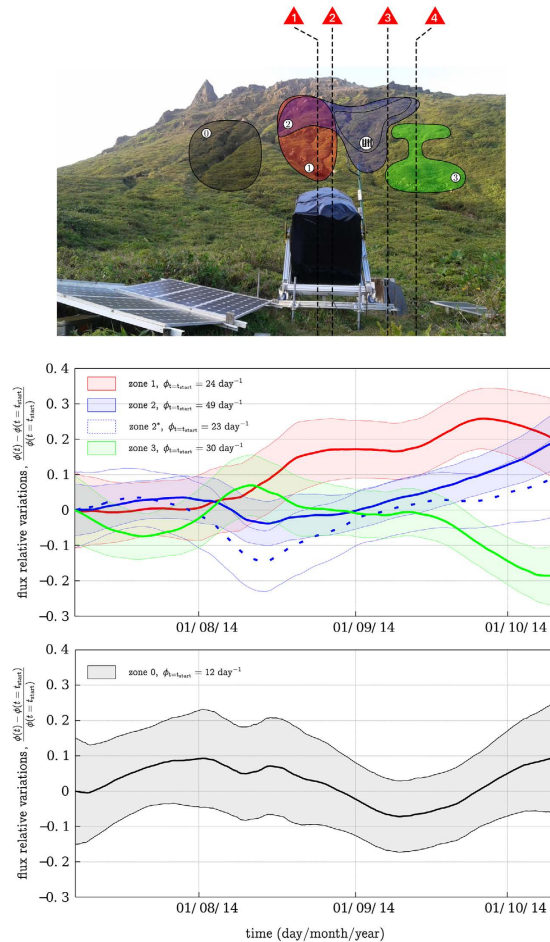
Figure 4. *Top: The La Soufrière of Guadeloupe as seen from the muon telescope.* The coloured regions refer to the regions from which we could extract coherent temporal signals. The red triangles refer to the different active zones visible at the surface of the dome azimuths (Fig. 1). *Middle:* The relative muon flux variations associated to the top picture regions $\varepsilon \in \{1, 2, 2^\star, 3\}$ during Summer 2014. The transparent surfaces associated to each curve delimit their respective uncertainty with a 95% confidence interval. The fluxes are computed using a 30 days large Hamming moving window. *Bottom:* Same as the middle graph for the control region ε_0.

The coefficients β_p^* and β_T^* are computed through linear regressions. They mainly depend on the measurement site altitude and latitude[37], and on the cut-off energy $E_c(\rho)$ corresponding to the screening caused by the amount ρ of matter facing the telescope[38], a primary importance in applications aiming at imaging large geological structures.

The barometric coefficient β_p^* is negative since an increase in p induces an increase in the air column opacity. It makes the atmosphere harder to go through for the muons and reduces their total flux. However it mainly affects the soft muons with an energy less than a few GeV. β_p^* is a decreasing function of E_c. This is due to the fact that the differential energy spectrum of cosmic muons is a sharply decreasing function. Consequently, as $E_c(\rho)$ increases, the number of low-energy muons stopped by an increase of atmosphere opacity is smaller. In the SHADOW experiment[29] where $E_c \approx 1\,$GeV, we got $\beta_p^* = 0.0013\ (0.0002)\ $hPa^{-1}. For the present experiment, the opacity ranges from 200 to 2000 mwe and $50 < E_c < 675\,$GeV. Numerous studies have measured or computed β_p^* for various cut-off energies[37,39], and in our case we have $\beta_p^*(E_c \gtrsim 50\,\text{GeV}) \lesssim 0.0001$. At the summit of the La Soufrière, $\overline{p} = 858\,$hPa and pressure variations $|p - \overline{p}| < 5\,$hPa. The associated muon flux relative variations are less than 0.1%, which is largely below the muon flux variations reported in Figs 3 and 4.

The second right-hand term of eq. 3 represents the temperature effect, which has already been parametrized multiple times in the literature[36,38,40]. We adopt here the parametrization of Barrett *et al.*[38,40] who define T_{eff} as the atmosphere temperature vertical average weighted by the cosmic pions disintegration probability. From the pions interaction probability with the atmosphere molecules (increasing with density) and their decay probability into muons (also affected by the local density), one expects β_T^* $[K^{-1}]$ negative for low energy particles (roughly[41] for E_c below 10 GeV), and positive for high energy particles.

For the la Soufrière de Guadeloupe experiment, we expect a negative α_T for the open-sky lines of sight, as most of the detected muons have a low energy and a positive α_T for the lines of sight crossing the volcano. Figure 5 shows the T_{eff} time series for the whole year 2014 in Guadeloupe using meteorological sounding balloons data. As
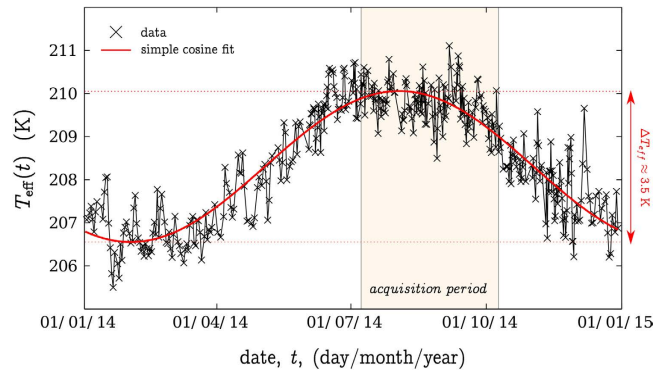
Figure 5. Effective temperature T_{eff} estimated from Le Raizet daily launched atmospheric sounding balloons (black crosses). The red curve is a simple fit using a cosine function. The data was extracted from the University of Wyoming website (http://weather.uwyo.edu/upperair/sounding.html).

can be observed, T_{eff} is well correlated with the seasons and it variations amplitude is about $\Delta T_{\text{eff}} \approx 3.5$ K. This value is very small because the Guadeloupe archipelago is close to the equator ($\lambda = 16.02°$ North) where seasonal effects are almost absent. It should be compared, for example, to the T_{eff} annual variation $\Delta T_{\text{eff}} \approx 42$ K observed at the ICECUBE detector in Antarctica ($\lambda = 89.59°$ South). For the ICECUBE experiment[42], $\alpha_T \approx -0.36$ for the open-sky muon flux ($E_c \approx 1$ GeV), and $\alpha_T \approx +0.90$ for high-energy muon flux ($E_c \approx 400$ GeV).

The present dataset being quite short, the sampling of T_{eff} annual variation is affected by large uncertainty: $\alpha_T = +1.05$ (1.45) (95% confidence interval) for the open-sky flux (Fig. 3 blue curve). Using the α_T values computed as a function of E_c through numerical models and measured with various underground experiments[41–44] (e.g. Fig. 7 from Adamson et al.[41]), we obtain $0.2 < \alpha_T < 0.8$ for the lava dome opacity range 200 mwe < 2000 mwe. With these values, the expected relative muon flux variations due to temperature effects should not exceed 0.3% during the acquisition period, which is more than one order of magnitude under the detected fluctuations (Fig. 3 red curve and Fig. 4).

From the results discussed in this section, we conclude that neither the pressure effects nor the temperature effects may explain a significant part of the muon flux variations observed through the lava dome.

Statistical time resolution. The temporal fluctuations one can extract from the muon flux signal are intrinsically limited by the statistical noise. We previously demonstrated[29] that the minimum acquisition time Δt_{min} necessary to extract a relative variation ε from the average detected flux ϕ_ε reads,

$$\Delta_t > \Delta t_{\text{min}} = \frac{\widetilde{\alpha}^2 \times (1 - \varepsilon^2/4)}{\varepsilon^2 \times \phi_\varepsilon},$$

(4)

with $\alpha = \text{erf}(\widetilde{\alpha})$ the confidence interval chosen to validate the statistical hypothesis.

A single observation axis that crosses the la Soufrière of Guadeloupe in this experiment detects between 1 and 5 particles per day. Then according to eq. 4 it can at best extract during our 95 days experiment a respectively 40 and 20% relative flux variation (with a 2σ precision). We could not detect such strong fluctuations in la Soufrière of Guadeloupe on this time-scale on a single axis. The solution is then to sum the signals from the different observation axes (see Methods section). Doing so we increase ϕ_ε, and improve both the time and amplitude resolutions of the fluctuations (respectively ε and Δt_{min}). As a counterpart, we deteriorate their spatial localization.

As presented on Fig. 4, we are finally able to extract $\varepsilon \approx 10\%$ relative fluctuations on a 30 days time-scale in regions regrouping from 21 (with zone ε_1) to 42 axes (with zone ε_2). Taking an average flux of 3 particles per day per observation axis, we respectively get with eq. 4 minimum acquisition times ranging from 13 to 24 days. These numbers are coherently below the 30 days Hamming window mentioned previously.

Discussion and Conclusions

The data presented and discussed in the preceding sections show that huge opacity variations occurred in the La Soufrière lava dome during Summer 2014. Using spatial PCA, theses variations revealed that the observed opacity changes are organized as separate regions located in the volcano southern half underneath the active fumarolic areas visible on the lava dome summit (Fig. 4). Both domains ε_1 and ε_2 show a conspicuous increase of their muon flux roughly starting August 1st for ε_1 and August 10th for ε_2. In the same period, a decrease of the muon flux through domain ε_3 starts August 8th. The only plausible explanation is that these rather fast mass changes originate from fluid movements inside the dome[45].

The muon flux variations, i.e. opacity fluctuations, in each domain may be used to estimate their associated mass changes. However, since the lines of sight are small conical volumes with their apex located on the telescope, the mass changes depend on the location of the concerned volume along the line of sight. We draw the entire volumes intercepted by the telescope for the 3 considered lines of sight subsets on Fig. 6. Let us assume that an opacity change $\Delta \varrho_m$ is observed for a given line of sight $\mathbf{r}_m$ and that a density variation $\delta\rho$ occurs somewhere in a volume V_m along this line. The segment length L_m of $V_m \cap \mathbf{r}_m$ reads (see eq. 1),
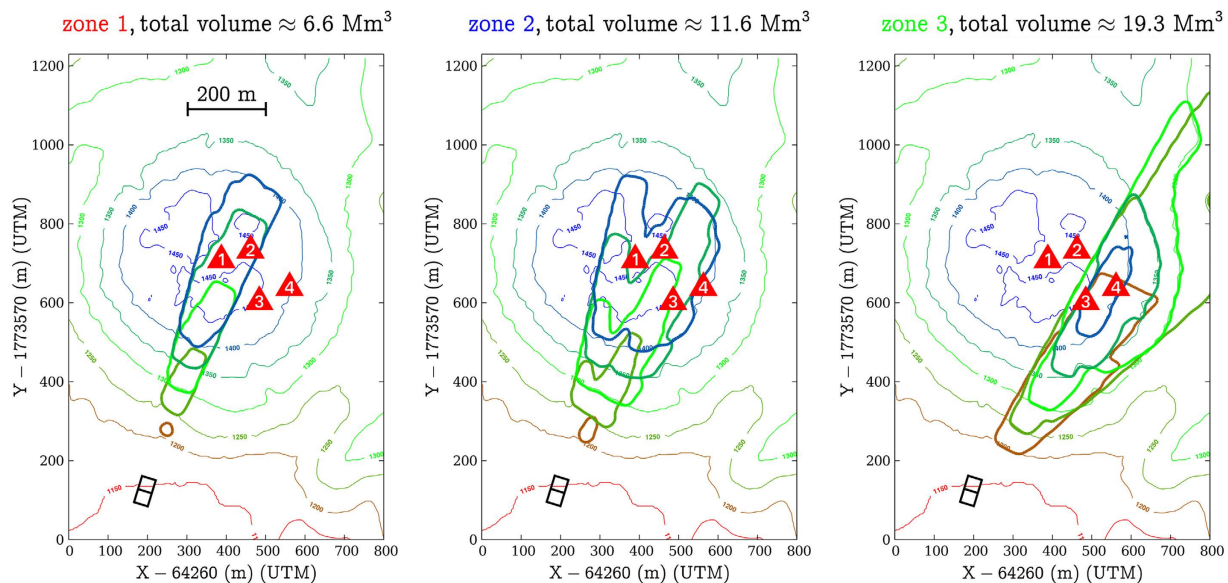
Figure 6. Plan view of the volume scanned by the muon telescope for the three domains ε_1, ε_2 and ε_3 represented on Fig. 4. The joined squares located SouthWest represent the telescope, and the red triangles refer to the active areas visible on the lava dome summit plateau (Fig. 1).
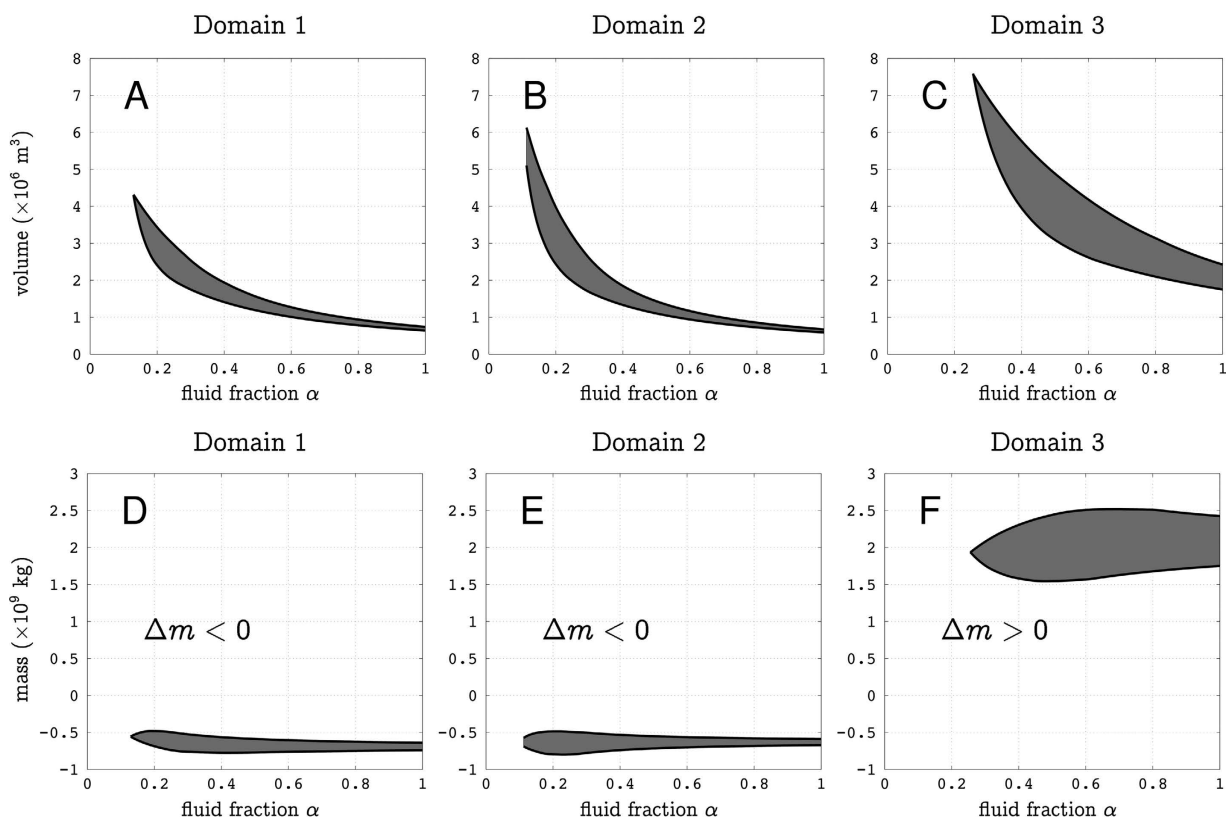

Figure 7. *Top*: Volume ranges V_ε for the domains ε_1 (**A**), ε_2 (**B**) and ε_3 (**C**) as a function of the fluid fraction α. *Bottom*: Ranges of mass change Δm_ε for the domains ε_1 (**D**), ε_2 (**E**) and ε_3 (**F**) as a function of the fluid fraction α.

$$L_m = \Delta \rho_m / \delta \rho. \tag{5}$$

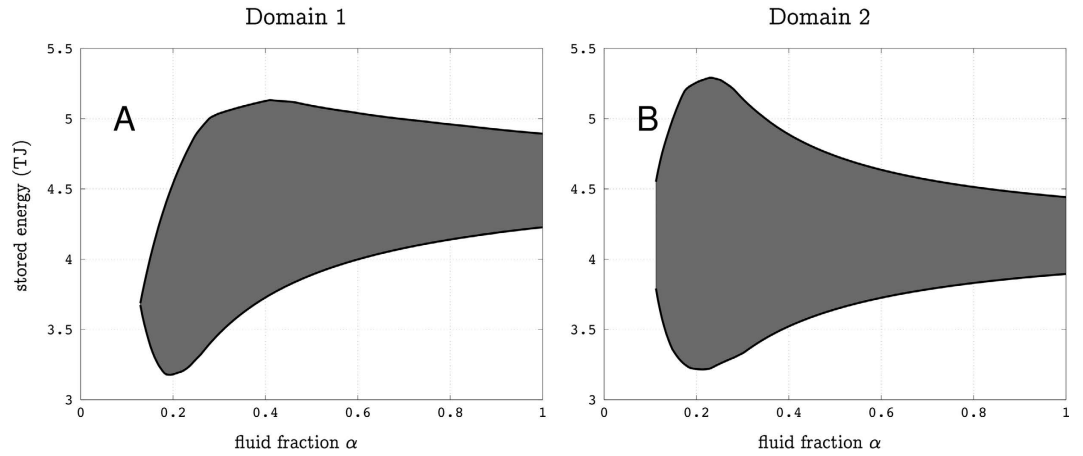If V_m is located at a distance L_0 from the telescope,

Domain 1   Domain 2

Figure 8. Energy brought by steam in domains ε_1 (**A**) and ε_2 (**B**) as a function of the fluid fraction α. Values computed for an absolute pressure p = 6 bars.

$$V_m = \Omega_m \int_{L_0-L_m/2}^{L_0+L_m/2} l^2 \mathrm{d}l, \tag{6}$$

where Ω_m is the small solid angle spanned by the line of sight $\mathbf{r}_m$. The total volume V_ε is obtained by summing the volumes of all lines of sight belonging to a given domain ε,

$$V_\varepsilon = \sum_{\mathbf{r}_m \in \varepsilon} V_m, \tag{7}$$

and the mass change associated with V_ε is given by,

$$\Delta m_\varepsilon = V_\varepsilon \times \delta\rho. \tag{8}$$

To compute the volumes V_ε and their corresponding mass changes Δm_ε, we need to know both $\delta\rho$ and L_0. The density change is assumed to be caused by fluid movements where liquid is replaced by gas (air or steam) or inversely. In such a case, $\delta\rho = \alpha \times 1000$ kg.m^{-3}, where α is the volume fraction occupied by the fluids in the rock matrix. The choice of L_0 may be guided by geological information about the locations where fluid movements are likely to occur inside the lava dome. In the present study, we consider that fluid movements occur under the active areas that occupy the Southern-East quarter of the summit plateau[45] (see the red triangles on Fig. 1). The volumes and mass changes corresponding to ε_1, ε_2 and ε_3 are shown in Fig. 7.

It may be expected that the positive mass variation of ε_3 (Fig. 7F) is due to the filling of a perched aquifer with rain water. Taking a surface $S = 1.5 \times 10^5$ m^2 for the summit plateau of the lava dome and a total amount of rain of 2 m during August and September, we obtain an upper bound of $S = 3 \times 10^8$ kg of water input on top the lava dome. However, most of this water is rapidly evacuated through run-off at the surface and it is very unlikely that filling ε_3 with rain water is the cause of the positive mass variation Δm_3. A more reasonable hypothesis is that this mass movement is due to fluid flow from ε_1 and ε_2 into ε_3. This is sustained by the fact that the positive mass variation Δm_3 is anti-correlated with the negative time-variations of mass associated with ε_1 and ε_2 (Fig. 4). Actually, the mass-variation ranges (Fig. 7) allow to have an almost vanishing mass budget, with the mass increase in ε_3 compensating the decreases in ε_1 and ε_2. In such a case, we expect that high-pressure steam formed in ε_1 and ε_2 and pushed liquid into ε_3. Considering that the steam pressure must be sufficient to push liquid and assuming a maximum reservoir depth of 50 m, we take an absolute pressure $p = 6$ bars. This gives a thermal energy storage of about 4.5×10^{12} J in each reservoir ε_1 and ε_2 (Fig. 8).

To conclude, PCA appears to be a fitted solution to regroup the telescope observation axes. We could extract 3 clear domains associated with various temporal signals that are probably linked to the different physical processes occurring into the volcano. PCA being a linear decomposition, it permits to consider an alignment of different zones on a single observation axis which is an intrinsic problem to tomography imaging from a single point of view. It is the case here with the zones ε_1 and ε_2 (Figs 4 and 9). The different domains geometrical shapes, as well as their alignment with the surface active vents are probably the best argument in favour of the detection of a volcanic signal because no prior information was injected into the analysis. ε_2 even shows a clear connection between two active regions.

However let us mention four factors that limit this approach. First our analysis assumes the temporal trends occur in fixed areas while we can expect the regions to change size, to merge in between each others, or to divide into smaller independent ones. Second the PCA algorithms searches the simplest possible solution. Many other combinations can be imagined, and for example two regions that completely superimpose onto the other as seen from the telescope cannot be distinguished (Fig. 4). Third PCA zoning may be biased by the telescope observation axes acceptance variations. The central axes have a higher sensitivity than the border ones[29,43]. This probably explains why we could not extract any fluctuations on the telescope scanning window borders (Fig. 9): the
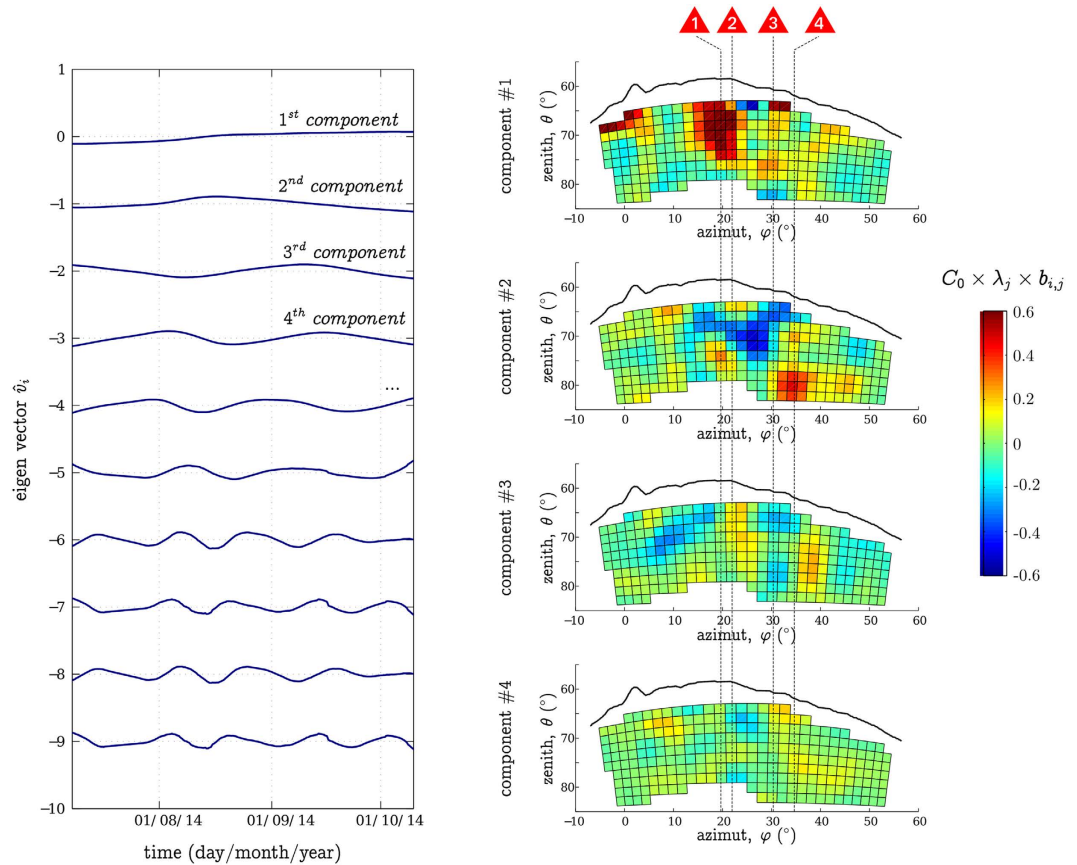
Figure 9. *Left*: **The first ten eigenvectors $\hat{v}_i$ extracted from the Summer 2014 muon tomography data.** All the eigenvectors should be centred but here we added an increasing offset so that the trends do not superimpose on each other. To construct them each observation axis was previously smoothed using a 30 days large Hamming moving window. *Right*: Graphical representation of the four first eigenvector contributions to the measured signal. Each box corresponds to an independent observation axis i and the associated color relates to $\lambda_j \times b_{i,j}$ (j going from 1 to 4). C_0 is a scaling constant. The black solid curve delimits the interface between the volcanic dome and the sky. The red triangles refer to the different active zones visible at the surface of the dome azimuths (Fig. 1).

associated axes have a weaker flux and thus a smaller weight in the PCA decomposition. Finally one could fear that when processed on such short data sets, PCA would tend to regroup observation axes with similar statistical noise. We believe it is not the case here as the regions presented on Fig. 4 are spatially coherent and aligned with the La Soufrière active vents, and because we detect fluctuations with a precision up to 4σ (see Fig. 4).

More constrains could be brought to the dynamics of the shallow hydrothermal system of the La Soufrière of Guadeloupe's lava dome with additionnal cosmic muon telescopes deployed around the volcano to provide radiographies taken under different angles of view, and also using recent 3D structural imaging of the volcanic dome[45]. This will allow to perform 3D reconstruction of the volumes ε_1, ε_2 and ε_3 and reduce the ranges of mass changes in Fig. 7. An even better reconstruction could be reached by merging the muon radiography measurements with continuous gravimetry data on the dome summit[46]. We estimated that the mass changes discussed in this study would generate gravity anomalies around a hundred microgal, which would be easy to measure with a standard gravimeter.

To conclude, we demonstrated that muon radiography provides unprecedented knowledge about the La Soufrière of Guadeloupe shallow hydrothermal system dynamics. We hope that it will become a standard geophysical monitoring technique to both improve our understanding of the physical processes at work and bring useful informations to assess hazard level. For example it could become a efficient proxy to localize pressurized reservoirs and evaluate their mechanical stability in order to prevent potential volcanic blasts.

Methods – Pixel merging through principal components analysis

As explained previously, a telescope single observation axis does not collect enough particles to statistically distinguish variations in the muon flux linked to the volcanic activity on a monthly time-scale. We can solve the problem regrouping various observation axes in order to increase the signal intensity. Thus, we come up with the following two-folds problematic: how to regroup the observation axes in order to efficiently extract temporal trends without introducing any prior information that may bias the solution ?

We propose here a solution using Principal Components Analysis (PCA, also called the Karhunen & Loeve Transformation[47,48]). Let us note $\mathbf{s}(t) = (s_1(t), s_2(t),..., s_N(t))$, where $\mathbf{s}(t)$ is a vector containing the Summer 2014 temporal signals $s_i(t)$ associated to the different observation axes that cross the volcano. PCA gives an optimal linear decomposition of the $s_i(t)$ on an orthonormal basis $\hat{\mathbf{s}}(t) = (\hat{s}_1(t), \hat{s}_2(t),..., \hat{s}_N(t))$ calculated iteratively from the signal itself,

- **Iteration 1:** we search $\hat{s}_1(t)$ such as,

$$\hat{s}_1(t) = \sum_{j=1}^{N} a_{1,j} \times s_j(t),$$

(9)

where the coefficients $a_{1,j}$ are estimated by minimizing the quadratic norm ε_1,

$$\varepsilon_1^2 = \sum_{j=1}^{N} \|\hat{s}_1(t) - s_j(t)\|^2.$$

(10)

- **Iteration i :** we search $\hat{s}_i(t)$ $(1 < i \leqslant N)$ such as,

$$\hat{s}_i(t) = \sum_{j=1}^{N} a_{i,j} \times s_j(t),$$

(11)

where the coefficients $a_{i,j}$ are estimated by minimizing the quadratic norm ε_i,

$$\varepsilon_i^2 = \sum_{j=1}^{N} \left\| \hat{s}_i(t) - \left(\sum_{k=1}^{i-1} s_j(t) - <s_j(t), \hat{s}_k(t)> \right) \right\|^2.$$

(12)

The resulting basis is orthogonal, we normalize it,

$$\hat{s}_i(t) = \lambda_i \times \hat{v}_i(t) , \quad \text{with} \quad <\hat{v}_i, \hat{v}_j> = \delta_{i,j},$$

(13)

where $\delta_{i,j}$ is the Kronecker Delta. $\hat{v}_i$ is the ith eigenvector and λ_i its associated eigenvalue.

Finally, usinq eqs 11 and 13 we get the decomposition,

$$s_i(t) = \sum_{j=1}^{N} \left(\lambda_j \times b_{i,j} \right) \times \hat{v}_j(t),$$

(14)

where $b_{i,j}$ are the square matrix $\mathbf{B}$ coefficients, with $\mathbf{B} = \mathbf{A}^{-1}$, $\mathbf{A}$ being the $N \times N$ square matrix associated to the $a_{i,j}$ coefficients.

Let us recall that PCA, as shown in eq. 12, assumes the signals $s_i(t)$ are affected by a Gaussian noise. This condition is not fulfilled for all the telescope observation axes going through the volcano, and for the time-scale we are interested in, because of the muon flux weak intensity. In order to overcome this problem, we merge observation axes into groups of four neighbours and the flux is computed with a 30 days large Hamming moving window.

By construction, the eigenvectors are less and less representative of the input data (λ_i is decreasing with i). Usually the first ones represent the global trends that are redundant on the different input signals while the last ones permit to reconstruct the little and specific discontinuities (mainly the noise). The eigenvectors are interesting four our study, because there is a possibility that they characterize different physical processes occurring inside the volcano, but we can also use the coefficients $b_{i,j}$ to map their respective contribution in the different regions of the dome.

Figure 9 shows the first ten eigenvectors (on the left) and, for the first four, their associated contribution on the different observation axes as seen from the telescope (on the right). Only the two first eigenvectors show fluctuations occurring on time-scales larger than a month, which can statistically be recovered considering the muon flux intensity (see the statistical time resolution section). The next eigenvectors present quicker fluctuations that characterize the statistical noise. Very clear large regions appear on the two first contribution maps (associated with the two first eigenvectors). The first component reveals a large coherent domain ε_1 aligned with the Tarissan pit (TP) and the North-Napoléon fume (NN). The second component shows two independent and anti-correlated regions: a V-shape zone ε_2 which left arm is aligned with TP and NN, and right arm with the Cratère Sud, the Gouffre Breislack (GB) and the Gouffre 56 (G56), and a bone-like zone ε_3 aligned with GB and G56. The next maps do not present any clear zone, the coefficients are small and appear to be randomly distributed in between the different observation axes (the little spatial coherence that appears is due to the neighbours merging mentioned previously).

References

1. Komorowski, J.-C. *et al.* Guadeloupe in *Volcanic Atlas of the Lesser Antilles*, (Seismic Research Unit, the University of the West Indies, Trinidad and Tobago*)*, 65–102 (2005).
2. Boudon, G. *et al.* Volcano flank instability in the Lesser Antilles Arc: Diversity of scale, processes, and temporal recurrence. *Journal of Geophysical Research* **112,** doi: 10.1029/2006JB004674 (2007).

3. Boudon, G., Komorowski, J.-C., Villemant, B. & Semet, M. P. A new scenario for the last magmatic eruption of La Soufrière of Guadeloupe (Lesser Antilles) in 1530 A.D. Evidence from stratigraphy radiocarbon dating and magmatic evolution of erupted products. *Journal of Volcanology and Geothermal Research* **178,** 474–490, doi: 10.1016/j.jvolgeores.2008.03.006 (2008).

4. Legendre, Y. Reconstruction fine de l'histoire èruptive et scènarii èruptifs *à* La Soufrière de Guadeloupe: vers un modèle intégré de fonctionnement du volcan (French) [A high resolution reconstruction of the eruptive past and definition of eruptive scenarii at La Soufrière of Guadeloupe] (University Paris 7 Ph.D. thesis, 2007).

5. Feuillard, M. *et al.* The 1975–1977 crisis of La Soufrière de Guadeloupe (F.W.I): a still-born magmatic erruption. *Journal o f Volcanology and Geothermal Research* **16,** 317–334; doi: 10.1016/0377-0273(83)90036-7 (1983).

6. Villemant, B. *et al.* Evidence for a new shallow magma intrusion at La Soufrière of Guadeloupe (Lesser Antilles). *Journal of Volcanology and Geothermal Research* **285,** 247–277, doi: 10.1016/j.jvolgeores.2014.08.002 (2014).

7. Allard, P. *et al.* Steam and gas emission rate from La Soufriere volcano, Guadeloupe (Lesser Antilles): Implications for the magmatic supply during degassing unrest. *Chemical Geology* **384,** 76–93, doi: 10.1016/j.chemgeo.2014.06.019 (2014).

8. Observatoire Volcanologique et Sismologique de Guadeloupe (IPGP). Bilan annuel 2014 de l'activité volcanique de la Soufrière de Guadeloupe et de la sismicité régionale (French) [The La Soufrière of Guadeloupe volcanic activity and regional seismicity 2014 annual summary] www.ipgp.fr/ovsg (2015).

9. Observatoire Volcanologique et Sismologique de Guadeloupe (IPGP). Bilan annuel 2015 de l'activité volcanique de la Soufrière de Guadeloupe et de la sismicité régionale (French) [The La Soufrière of Guadeloupe volcanic activity and regional seismicity 2015 annual summary] www.ipgp.fr/ovsg (2016).

10. Hurst, T., Jolly, A. D. & Sherburn, S. Precursory characteristics of the seismicity before the 6 August 2012 eruption of Tongariro volcano, North Island, New Zealand. *Journal of Volcanology and Geothermal Research* **286,** 294–302; doi: 10.1016/j.jvolgeores.2014.03.004 (2014).

11. Jolly, G., Keys, H., Procter, J. & Deligne, N. Overview of the co-ordinated risk-based approach to science and management response and recovery for the 2012 eruptions of Tongariro volcano, New Zealand. *Journal of Volcanology and Geothermal Research* **286,** 184–207; doi: 10.1016/j.jvolgeores.2014.08.028 (2014).

12. Lube, G. *et al.* Dynamics of surges generated by hydrothermal blasts during the 6 August 2012 Te Maari eruption, Mt. Tongariro, New Zealand. *Journal of Volcanology and Geothermal Research* **286,** 348–366; doi: 10.1016/j.jvolgeores.2014.05.010 (2014).

13. Cyranoski, D. Why Japan missed volcano's warning signs. *Nature News*; doi: 10.1038/nature.2014.16022 (2014).

14. Kato, A. *et al.* Preparatory and precursory processes leading up to the 2014 phreatic eruption of Mount Ontake, Japan. *Earth, Planets and Space* **67,** doi: 10.1186/s40623-015-0288-x (2015).

15. Maeda, Y. *et al.* Source mechanism of a VLP event immediately before the 2014 eruption of Mt. Ontake, Japan. *Earth, Planets and Space* **67,** 1–11, doi: 10.1186/s40623-015-0358-0 (2015).

16. Sano, Y. *et al.* Ten-year helium anomaly prior to the 2014 Mt Ontake eruption. *Scientific Reports* **5,** 13069; doi: 10.1038/srep13069 (2015).

17. George, E. P. Cosmic rays measure overburden of tunnel. *Commonwealth Engineer*, 455–457 (1955).

18. Alvarez, L. W. *et al.* Search for hidden chambers in the pyramids. *Science* **167,** 832–839, doi: 10.1126/science.167.3919.832 (1970).

19. Nagamine, K. *Introductory muon science* (Cambridge University Press, (2003).

20. Tanaka, H. K. Subsurface density mapping of the earth with cosmic ray muons. Nuclear Physics B - Proceedings Supplements **243–244,** 239–248; doi: 10.1016/j.nuclphysbps.2013.09.020 (2013).

21. Gaisser, T. *Cosmic rays and particle physics* (Cambridge University Press, (1990).

22. Lesparre, N. *et al.* Geophysical muon imaging: feasibility and limits. *Geophysical Journal International* **183,** 1348–1361; doi: 10.1111/j.1365-246X.2010.04790.x (2010).

23. Tang, A., Horton-Smith, G., Kudryavtsev, V. A. & Tonazzo, A. Muon simulations for Super-Kamiokande, KamLAND, and CHOOZ. *Physical Review D* **74,** 053007; doi: 10.1103/PhysRevD.74.053007 (2006).

24. Tanaka, H. K. M. *et al.* Imaging the conduit size of the dome with cosmic-ray muons: The structure beneath Showa-Shinzan Lava Dome, Japan. *Geophysical Research Letters* **34,** 053007; doi: 10.1029/2007GL031389 (2007).

25. Lesparre, N. *et al.* Density muon radiography of La Soufrière of Guadeloupe volcano: comparison with geological, electrical resistivity and gravity data: Density muon radiography of La Soufrière, Guadeloupe. *Geophysical Journal International* **190,** 1008–1019; doi: 10.1111/j.1365-246X.2012.05546.x (2012).

26. Gibert, D. *et al.* Density muon tomography of La Soufrière of Guadeloupe lava dome. Oral presentation at IAVCEI 2013 Scientific Assembly, Kagoshima, Japan, 2013.

27. Tanaka, H. K. M., Kusagaya, T. & Shinohara, H. Radiographic visualization of magma dynamics in an erupting volcano. *Nature Communications* **5,** 3381; doi: 10.1038/ncomms4381 (2014).

28. Lesparre, N. *et al.* Design and operation of a field telescope for cosmic ray geophysical tomography. *Geoscientific Instrumentation, Methods and Data Systems* **1,** 33–42; doi: 10.5194/gi-1-33-2012 (2012).

29. Jourde, K. *et al.* Monitoring temporal opacity fluctuations of large structures with muon radiography: a calibration experiment using a water tower. *Scientific Reports* **6,** 23054; doi: 10.1038/srep23054 (2016).

30. Nishiyama, R. *et al.* Experimental study of background noise in muon radiography using emulsion film detectors. *Geoscientific Instrumentation Methods and Data Systems* **3,** 29–39; doi: 10.5194/gi-3-29-2014 (2014).

31. Ambrosino, F. *et al.* Joint measurement of the atmospheric muon flux through the Puy de Dôme volcano with plastic scintillators and Resistive Plate Chambers detectors. *Journal of Geophysical Research: Solid Earth* **120,** 7290–7307; doi: 10.1002/2015JB011969 (2015).

32. Nishiyama, R. *et al.* Monte Carlo simulation for background study of geophysical inspection with cosmic-ray muons. *Geophysical Journal International* **206,** 1039–1050; doi: 10.1093/gji/ggw191 (2016).

33. Jourde, K. *et al.* Experimental detection of upward going cosmic particles and consequences for correction of density radiography of volcanoes. *Geophysical Research Letters* **40,** 6334–6339; doi: 10.1002/2013GL058357 (2013).

34. Marteau, J. *et al.* Implementation of sub-nanosecond time-to-digital converter in field-programmable gate array: applications to time-of-flight analysis in muon radiography. *Measurement Science and Technology* **25,** 035101; doi: 10.1088/0957-0233/25/3/035101 (2014).

35. Blackett, P. M. On the instability of the barytron and the temperature effect of cosmic rays. *Physical Review* **54,** 973; doi: 10.1103/PhysRev.54.973 (1938).

36. Duperier, A. A new cosmic-ray recorder and the air-absorption and decay of particles. *Terrestrial Magnetism and Atmospheric Electricity* **49,** 1–7; doi: 10.1029/TE049i001p00001 (1944).

37. Motoki, M. *et al.* Precise measurements of atmospheric muon fluxes with the BESS spectrometer. *Astroparticle Physics* **19,** 113–126; doi: 10.1016/S0927-6505(02)00195-0 (2003).

38. Barrett, P. H., Bollinger, L. M., Cocconi, G., Eisenberg, Y. & Greisen, K. Interpretation of cosmic-ray measurements far underground. *Reviews of Modern Physics* **24,** 133; doi: 10.1103/RevModPhys.24.133 (1952).

39. Sagisaka, S. Atmospheric effects on cosmic-ray muon intensities at deep underground depths. *Il Nuovo Cimento* **9,** 809–828; doi: 10.1007/BF02558081 (1986).

40. Barrett, P., Cocconi, G., Eisenberg, Y. & Greisen, K. Atmospheric temperature effect for mesons far underground. *Physical Review* **95,** 1573–1575; doi: 10.1103/PhysRev.95.1573 (1954).

41. Adamson, P. *et al.* Observation of muon intensity variations by season with the MINOS far detector. *Physical Review D* **81,** 012001; doi: 10.1103/PhysRevD.81.012001 (2010).
42. Tilav, S. *et al.* Atmospheric Variations as observed by IceCube. *arXiv preprint*; arXiv:1001.0776 (2010).
43. Lesparre, N., Gibert, D. & Marteau, J. Bayesian dual inversion of experimental telescope acceptance and integrated flux for geophysical muon tomography. *Geophysical Journal International* **188,** 490–497; doi: 10.1111/j.1365-246X.2011.05268.x (2012).
44. Ambrosio, M., Antolini, R. & Auriemma, G. Seasonal variations in the underground muon intensity as seen by MACRO. *Astroparticle Physics* textbf **7,** 109–124; doi: 10.1016/S0927-6505(97)00011-X (1997).
45. Rosas-Carbajal, R., Komorowski, J.-C., Nicollin, F. & Gibert, D. Volcano electrical tomography unveils edifice collapse hazard linked to hydrothermal system structure and dynamics. *Scientific Reports* **6,** 29899; doi: 10.1038/srep29899 (2016).
46. Jourde, K., Gibert, D. & Marteau, J. Improvement of density models of geological structures by fusion of gravity data and cosmic muon radiographies. *Geoscientific Instrumentation Methods and Data Systems* **4,** 177–188; doi: 10.5194/gi-4-177-2015 (2015).
47. Pearson, K. On lines and planes of closest fit to systems of points in space. *The London, Edinburgh, and Dublin Philosophical Magazine and Journal of Science* **2,** 559–572 (1901).
48. Lebart, L., Piton, M. & Morineau, A. *Statistique exploratoire multidimensionnelle* (ed. Dunod, Paris, 2006).

Acknowledgements

Author Contributions

K.J., J.M. and D.G. conceived the experiment; K.J., J.M., D.G. and J.D.B. designed and constructed the apparatus; K.J., D.G. and J.M. conducted the experiment; K.J., J.M. and D.G. analysed the data; all authors wrote the article.

Additional Information

Competing financial interests: The authors declare no competing financial interests.

How to cite this article: Jourde, K. *et al.* Muon dynamic radiography of density changes induced by hydrothermal activity at the La Soufrière of Guadeloupe volcano. *Sci. Rep.* **6,** 33406; doi: 10.1038/srep33406 (2016).